

Mean First Passage Time for Persistent Random Walks in Annular Search Domains *

Fatemeh Saghafifar[†] and Daniel Coombs[‡]

Abstract. We study the mean first-passage time of a random walker to a small absorbing target at the center of a two-dimensional annulus with a specularly reflecting outer boundary. The problem is motivated by natural killer cell migration toward a target cancer cell, where the goal is to quantify how long it takes immune cells to reach the target and how search efficiency depends on directional persistence and chemotactic bias. Cell motion is modeled as a velocity-jump process. We first consider a correlated random walk with a von Mises turning kernel, with a concentration parameter controlling directional persistence. We then extend the model to a biased correlated random walk using a phase-shifted turning kernel that represents preferential motion, for example following a concentration gradient. Our analysis combines closed-form benchmarks for simple and biased random walks, Fourier-mode reductions of the transport equations for the correlated and biased correlated models, and a fast-turning perturbation expansion that gives an analytical correction to the diffusion-limit mean first-passage time for the random walker. Our analytical results are supported by numerical methods that include a semi-Lagrangian solver in radial and angular coordinates, a stationary discretisation designed to handle biased transport, and an event-driven Monte Carlo simulator for cross-validation. Together, our results provide a framework relating persistent and biased immune-cell motion to target-search times in confined two-dimensional domains.

Key words. mean first-passage time, persistent random walk, correlated random walk, biased correlated random walk

MSC codes. 92-10; 92C17; 70-10; 60K40

1. Introduction. Many cell movements exhibit directional persistence: bacteria run and tumble [5, 4], T cells and neutrophils alternate between smooth runs with sudden turns [36, 27], fibroblasts and *Dictyostelium* retain memory of their direction over minutes [14, 43], and keratocytes provide an example of highly persistent cell migration with trajectories that remain close to ballistic [13, 32, 28]. One biologically important quantity in all these scenarios is the first-passage time to a target, such as an antigen-presenting cell, a chemical source, or a wound edge, under stochastic cell-migration dynamics.

The usual random walk models, simple random walks (SRWs) and biased random walks (BRWs), are widely used in mathematical biology to describe single-cell tracking data and can yield closed-form mean first passage time (MFPT) formulae in radially symmetric geometries [40, 38, 39]. However, these models do not distinguish between two different sources of directed motion: directional persistence, which arises from a walker’s internal memory of its previous direction, and external bias, which arises from cues such as chemical gradients. This distinction is important because the underlying stochastic process, and therefore the result-

*

Funding: This work was supported by the Natural Sciences and Engineering Research Council of Canada.

[†]Department of Mathematics and Institute of Applied Mathematics, University of British Columbia, 1984 Mathematics Road, Vancouver, BC, V6T 1Z2, Canada (fsaghafi@math.ubc.ca).

[‡]Department of Mathematics and Institute of Applied Mathematics, University of British Columbia, 1984 Mathematics Road, Vancouver, BC, V6T 1Z2, Canada (coombs@math.ubc.ca).

ing search dynamics, depends on how directional information is introduced. The correlated random walk (CRW) accounts for directional persistence by sampling turning angles from a non-uniform distribution, typically the von Mises distribution [35, 11]. The corresponding backward equation is a transport equation in position-velocity space, rather than a diffusion equation in position space alone, and it admits no closed-form MFPT in confined geometries.

Related work on MFPT for non-diffusive motion has been developed along two main lines: For velocity-jump and active-particle models, recent results include a general transport-MFPT framework by Hillen, D’Orsogna, Mantooth, and Lindsay [22], its recent extension to higher dimensions with directional bias by D’Orsogna, Lindsay, and Hillen [12], and a MFPT analysis for active Brownian particles in two dimensions by Iyaniwura and Peng [26]. Earlier work in this direction includes the quasi-steady-state analysis of motor-driven transport on two-dimensional microtubular networks by Bressloff and Newby [7], and the asymptotic narrow-capture analysis of first-passage problems in ecological settings by Kurella, Tzou, Coombs, and Ward [30]. For diffusive motion in domains with small targets, the narrow-capture problem has an extensive literature; for reviews see Holcman and Schuss [25] and the book by Grebenkov, Metzler, and Oshanin [17]. This literature covers the MFPT and its full distribution, including the variance [15], multi-target configurations with mixed boundary conditions [18], trap-placement optimization [9], and the extreme first-passage time of the fastest among multiple independent walkers competing to reach a target [31, 16].

Here, we address a complementary regime: rather than studying diffusive searchers in domains with small absorbing windows, we consider a velocity-jump process in which persistence and chemotactic bias are introduced separately and their combined effect on MFPT is quantified through the correlated and biased-correlated random walk pair. To focus on the main issues, we study a simplified but representative geometry: the two-dimensional annulus $a < |\mathbf{x}| < R$, with an absorbing inner boundary and a specularly reflecting outer boundary.

In this setting, we present several several new results relevant to biological modelling:

- (i) We derive analytical limits of the CRW MFPT in the fast turning and strong persistence regimes, and compute a closed-form expression for the persistence-induced reduction in search time via a leading-order perturbation correction to the diffusion-limit MFPT. This correction arises from a kinetic boundary layer at the absorbing target, rather than from a bulk correction in the interior.
- (ii) We present a chemotactic extension model in which persistence and external bias act together, represented here by a biased correlated random walk (BCRW).
- (iii) We develop a semi-Lagrangian numerical solver for the CRW MFPT in confined geometries which resolves a persistence-induced outer wall layer. We characterize the solver’s structural accuracy ceiling through eigenpair analysis and Richardson extrapolation, and replace it with a stationary formulation that eliminates this ceiling. We then extend the solver to the BCRW and validate against an event-driven Monte Carlo simulator and ballistic regime predictions from the ecological random walk literature [10, 11].

Together, our results show that directional persistence reduces the confined search time monotonically over the biologically relevant parameter range, with diminishing additional benefit at high persistence.

The paper is organized as follows. [Section 2](#) sets up the geometry, the backward Fokker–

Abbreviation	Model
SRW	Simple Random Walk (diffusive motion)
BRW	Biased Random Walk (e.g. SRW with chemoattractants)
CRW	Correlated Random Walk (e.g. SRW with persistent motion)
BCRW	Biased Correlated Random Walk (full model)

Table 1: Abbreviated model names

Planck equation, and the CRW and BCRW transport equations. [Section 3](#) summarizes a number of useful analytical results: a double-integral MFPT formula for the SRW and BRW which serves as a useful benchmark; fast-turning and strong-persistence limits of the CRW; a Fourier-mode approach to the CRW and BCRW problems; and finally the leading-order perturbation correction to the diffusion-limit MFPT for the CRW. [Section 4](#) describes the CRW semi-Lagrangian solver, the BCRW extension, and the Monte Carlo benchmark. [Section 5](#) reports verification, graded-mesh convergence, eigenpair analysis, Richardson extrapolation, and the documented $\sim 2.7\%$ structural ceiling. [Section 6](#) provides a rough calibration of κ using data from different classes of cells and reports a worked prediction for T cells. Finally, [Section 7](#) states the main verified result and [Section 8](#) interprets the findings and describes possible future work.

2. Problem formulation. We formulate the target-search problem in a two-dimensional annular domain

$$D = \{ \mathbf{x} \in \mathbb{R}^2 : a < |\mathbf{x}| < R \},$$

where the inner boundary $r = a$ is absorbing and represents the target, such as a tumour or a cancer cell, while the outer boundary $r = R$ is reflecting and represents confinement by the surrounding tissue or an experimental domain. This geometry provides a simplified model of a confined search process in which a motile cell moves within a bounded region, and first passage occurs when the cell reaches the central target ([Figure 1](#)).

Mean First Passage Time backward formulation. We first recall the standard backward formulation for Brownian motion-based models. For a time-homogeneous stochastic differential equation

$$dX_t = b(X_t) dt + \sigma(X_t) dW_t$$

on a bounded domain $D \subset \mathbb{R}^2$, the infinitesimal generator acting on smooth test functions $f(X_t)$ is defined as

$$\mathcal{L}f = b \cdot \nabla f + \left(\frac{1}{2} \sigma \sigma^\top \right) : \nabla^2 f.$$

This operator is used to derive the mean first-passage time of the stochastic process which is defined as

$$T(\mathbf{x}) = \mathbb{E}[\inf\{t > 0 : X_t \in \partial D\} \mid X_0 = \mathbf{x}],$$

and satisfies the backward Fokker–Planck equation

$$(2.1) \quad \mathcal{L}T(\mathbf{x}) = -1, \quad \mathbf{x} \in D,$$

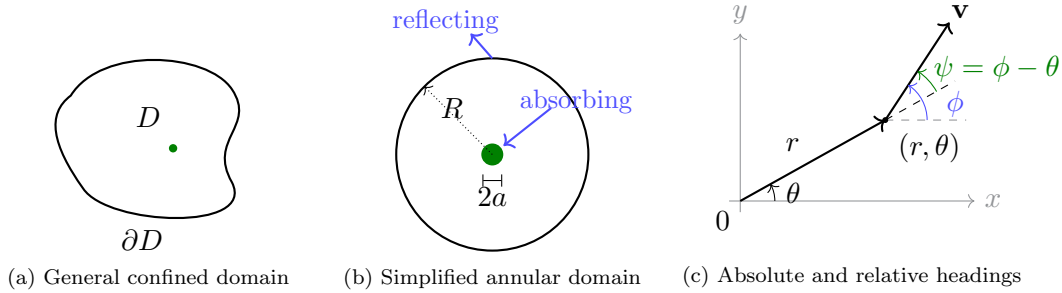


Figure 1: Schematic of the search problem. (a) A general confined domain with an absorbing small target (green node). (b) The simplified annular geometry, where the inner boundary $r = a$ is absorbing and the outer boundary $r = R$ is specularly reflecting. (c) Definition of the absolute heading ϕ , polar angle θ , and relative heading $\psi = \phi - \theta$.

with $T = 0$ on the absorbing boundary and a homogeneous Neumann condition on any reflecting boundary [39].

Velocity-jump process and turning kernel. To model directional persistence, we replace the diffusion process with a velocity-jump process, which retains information about the walker's previous direction. The walker moves at constant speed s in heading direction ϕ . Turning events occur as a Poisson process with rate μ , and after each event the new heading is sampled from a turning kernel $K(\phi | \phi')$, where ϕ' is the heading before the turn. Between turning events, the walker follows straight-line motion at speed s .

Because the target and outer boundary are concentric, polar coordinates are the natural choice. The boundaries are simply $r = a$ and $r = R$, and the relative heading $\psi = \phi - \theta$ separates radial motion toward or away from the target from tangential motion around it.

For the (unbiased) correlated random walk (CRW), the turning kernel depends only on the turning angle $\eta = \phi - \phi'$. Since headings are angular variables defined on the circle, the turning-angle distribution should also be circular. We therefore use the von Mises distribution, which is the circular analogue of the normal distribution:

$$(2.2) \quad K(\eta; \kappa) = \frac{1}{2\pi I_0(\kappa)} \exp(\kappa \cos \eta), \quad \eta = \phi - \phi'.$$

Here $\kappa \geq 0$ is the concentration parameter, and the normalization contains I_n , the modified Bessel function of the first kind of order n . The parameter κ controls the directional persistence of the walk. The walk's first trigonometric moment is

$$c = \langle \cos \eta \rangle = \frac{I_1(\kappa)}{I_0(\kappa)},$$

so $\kappa = 0$ gives an isotropic turning distribution, while larger κ corresponds to stronger directional memory [10, 11, 35]. Because K depends only on the turning angle $\eta = \phi - \phi'$ and cosine is an even function, the kernel is symmetric under interchange of its pre- and post-turn headings and is therefore self-adjoint; the adjoint kernel K^* has the same functional form as (2.2).

In the unbiased case, rotational symmetry implies that the mean first-passage time depends only on the radius r and the relative heading $\psi = \phi - \theta$, so we write $T = T(r, \psi)$. The deterministic motion between turning events gives the advection part of the backward operator. Since the walker moves at speed s in the absolute heading direction ϕ , the polar-coordinate rates are

$$\frac{\partial r}{\partial t} = s \cos \psi, \quad \frac{\partial \theta}{\partial t} = \frac{s}{r} \sin \psi, \quad \frac{\partial \phi}{\partial t} = 0,$$

and the relative heading satisfies

$$\frac{\partial \psi}{\partial t} = \frac{\partial \phi}{\partial t} - \frac{\partial \theta}{\partial t} = -\frac{s}{r} \sin \psi.$$

Turning events occur at rate μ . At a turning event, the current value of $T(r, \psi)$ is replaced by its average over post-turn headings weighted by the turning kernel, expressed in the relative-heading variable as $K(\psi - \psi'; \kappa)$. Combining the deterministic streaming terms, the turning operator, and the fact that time accumulates at unit rate before absorption, we obtain the backward transport equation

$$(2.3) \quad -1 = s \cos \psi \partial_r T - \frac{s \sin \psi}{r} \partial_\psi T - \mu T + \mu \int_0^{2\pi} K(\psi - \psi'; \kappa) T(r, \psi') d\psi'.$$

The inner boundary condition is that $T(a, \psi) = 0$ for inward-pointing headings. At the outer boundary, we set $T(R, \psi) = T(R, \pi - \psi)$. The outer condition states that, upon contact with the reflecting wall, the radial component of velocity changes sign while the tangential component is preserved.

Biased Correlated random walk and chemotaxis. To include chemotactic bias in addition to persistence, we introduce a biased correlated random walk. Motivated by biased and correlated random walk formulations in the biological movement literature [10, 11, 40], we introduce bias by shifting the turning distribution toward a preferred direction $\phi_0(r, \theta)$, which represents the local direction of an external cue such as a chemical gradient produced by the target. The bias strength is denoted by d_τ . A phase-shifted von Mises kernel is used:

$$(2.4) \quad K(\phi | r, \theta, \phi') = \frac{1}{2\pi I_0(\kappa)} \exp[\kappa \cos(\phi - \phi' + d_\tau(\phi - \phi_0(r, \theta)))].$$

When $d_\tau = 0$, this reduces to the unbiased correlated random walk kernel. When $d_\tau \neq 0$, the new heading is influenced both by the previous heading, through persistence, and by the external bias direction, through the phase shift.

Because the preferred direction may depend on position, the biased model is no longer rotationally invariant in the same reduced variables unless the biasing (cue) field has special symmetry. We therefore write the mean first-passage time as $T = T(r, \theta, \phi)$. The backward transport equation for the biased correlated random walk is

$$(2.5) \quad -1 = s \cos(\phi - \theta) \partial_r T + \frac{s \sin(\phi - \theta)}{r} \partial_\theta T - \mu T + \mu \int_0^{2\pi} K^*(\phi, \phi', r, \theta) T(r, \theta, \phi') d\phi',$$

where the adjoint kernel is obtained by swapping the pre-turn and post-turn headings,

$$K^*(\phi, \phi', r, \theta) = K(\phi' | r, \theta, \phi).$$

The absorbing condition at the target is

$$(2.6) \quad T(a, \theta, \phi) = 0 \quad \text{for headings that enter the target,}$$

and the specular reflection condition at the outer boundary, based on calculations shown in [Section B](#), will be

$$(2.7) \quad T(R, \theta, \phi) = T(R, \theta, 2\theta + \pi - \phi).$$

This condition is the angular form of specular reflection: the outgoing heading is obtained by reflecting the incoming velocity across the tangent line at the boundary.

Model hierarchy. The simple random walk, biased random walk, correlated random walk, and biased correlated random walk therefore form a hierarchy of models. The simple and biased random walks provide diffusion-based benchmark problems for which closed-form radial mean first-passage times can be derived. The correlated random walk introduces directional memory and leads to a transport equation in position-heading space. The biased correlated random walk further includes external directional cues and provides the framework used below to study the combined effect of persistence and chemotactic bias on search time.

3. Analytical results.

3.1. Simple and Biased Random Walk.

A unified double-integral formula. We begin with a simple diffusion-based model. For the constant diffusivity simple random walk, with stochastic differential equation written as

$$dX_t = \sqrt{2D} dW_t,$$

the backward Fokker–Planck equation [\(2.1\)](#) reduces, under radial symmetry, to

$$D \left(u''(r) + \frac{1}{r} u'(r) \right) = -1, \quad u(a) = 0, \quad u'(R) = 0.$$

Solving this boundary value problem gives

$$(3.1) \quad u_{\text{SRW}}(r) = \frac{R^2}{2D} \ln \frac{r}{a} + \frac{a^2 - r^2}{4D}.$$

The same calculation extends to a biased random walk with radial drift and possibly anisotropic diffusivities. If the radial drift is written as $-\mu(r)\mathbf{e}_r$ and the radial and angular diffusivities are $D_r(r)$ and $D_\theta(r)$, respectively, then the radial mean first passage time satisfies

$$D_r(r)u''(r) + \left(\frac{D_\theta(r)}{r} - \mu(r) \right) u'(r) = -1.$$

Writing $w = u'$ gives a first-order linear equation for w . Defining

$$P(r) = \frac{D_\theta(r)/r - \mu(r)}{D_r(r)}, \quad M(r) = \exp\left(\int^r P(q) dq\right),$$

and using the reflecting condition $u'(R) = 0$, we obtain

$$(3.2) \quad u_{\text{BRW}}(r) = \int_a^r \frac{1}{M(t)} \int_t^R \frac{M(s)}{D_r(s)} ds dt.$$

This double-integral representation provides a common benchmark for the constant and variable coefficient simple and biased random walk cases used in this paper. In particular, the constant drift, isotropic diffusion biased random walk is recovered as a special case and can also be written in terms of exponential integral functions.

Numerical finite difference methods for the simple diffusion-based walks (SRW and BRW) are described in [Section A](#).

Fast-turning diffusion limit. We next consider the fast-turning limit of the correlated random walk. In this regime, turning events occur frequently compared with the time scale of target search, so the transport process can be approximated by an effective diffusion. A moment closure of the forward CRW equation gives the following macroscopic density equation [\[22, 23\]](#).

$$(3.3) \quad \partial_t \rho = D_{\text{eff}} \Delta \rho, \quad \text{where} \quad D_{\text{eff}} = \frac{s^2}{2\mu(1 - m_1)} \quad \text{and} \quad m_1 = \frac{I_1(\kappa)}{I_0(\kappa)}.$$

The same diffusion-limit equation arises as the unbiased, fast-turning limit of the general higher-dimensional velocity-jump MFPT framework of reference [\[12\]](#), in the radially symmetric unbiased case. The leading-order mean first passage time is therefore the SRW [\(3.1\)](#) with $D = D_{\text{eff}}$. This diffusion approximation provides the reference solution used below to measure the effect of finite turning rate and directional persistence on the CRW MFPT.

Strong-persistence limit. We also record the limiting form of the correlated random walk when directional persistence is strong. As the concentration parameter κ tends to infinity, the von Mises kernel concentrates near zero turning angle and is locally Gaussian with variance $1/\kappa$. In this limit, the turning operator is approximated by angular diffusion, so that

$$\mu \int_0^{2\pi} K^*(\psi, \psi') T(r, \psi') d\psi' - \mu T(r, \psi) \approx D_\psi \partial_{\psi\psi} T, \quad \text{where} \quad D_\psi = \frac{\mu}{\kappa}.$$

Thus [Equation \(2.3\)](#) approaches a drift–diffusion equation in the heading variable, closely related to the backward equations used for active Brownian particles [\[26\]](#). The leading-order motion is nearly deterministic between rare changes in heading, so the MFPT approaches the straight-line hitting time when the initial orientation intersects the target. In the annular problem, this limit is modified by specular reflection at the outer boundary. The near-ballistic regime also develops a thin boundary layer in heading space, which is a common feature of strongly persistent velocity-jump processes. This is also the regime in which our semi-Lagrangian numerical solver begins to lose angular resolution (scenarios presented in [Section 5](#)).

Reduction of the CRW Fourier hierarchy. We next reduce the unbiased transport equation by using the periodicity of the heading variable. Since the von Mises kernel depends only on the turning angle, it acts as a convolution operator on the circle. Expanding

$$T(r, \psi) = \sum_{n \in \mathbb{Z}} u_n(r) e^{in\psi},$$

the convolution is diagonal in Fourier space, with multipliers given by the normalized moments of the von Mises distribution,

$$(3.4) \quad (K * T)(\psi) = \sum_{n \in \mathbb{Z}} m_n u_n(r) e^{in\psi}, \quad m_n = \frac{I_n(\kappa)}{I_0(\kappa)}.$$

This diagonalization is the circular analogue of using Fourier modes for translation invariant kernels and follows from the standard Fourier representation of the von Mises distribution [35, 24].

Substituting this expansion into Equation (2.3) and matching coefficients of $e^{in\psi}$ gives the infinite coupled hierarchy

$$(3.5) \quad -\delta_{n,0} = \frac{s}{2}(u'_{n-1} + u'_{n+1}) + \frac{s}{2r}((n-1)u_{n-1} + (n+1)u_{n+1}) + \mu(m_n - 1)u_n.$$

The coupling between neighboring modes comes from the factors $\cos \psi$ and $\sin \psi$ in the advection part of the transport equation, while the turning operator remains diagonal in mode space. The absorbing condition gives $u_n(a) = 0$ for all n , and specular reflection at the outer boundary gives

$$u_n(R) = (-1)^n u_{-n}(R).$$

This hierarchy is useful analytically because it makes explicit how directional persistence enters through the multipliers m_n . It also provides a diagnostic check on the numerical transport solver. In this work, however, truncated-Fourier versions of Equation (3.5) are not used as the primary solver. Direct truncations led to structural difficulties that are summarized in Section D. We therefore use the hierarchy for analysis and verification, while the main computations are carried out with the stationary transport discretization described in Section 4.

Reduction of the BCRW Fourier hierarchy. We next explore how the biased turning operator appears in mode space. This reduction will not be used as the primary numerical solver, but it is useful for checking the structure of the biased correlated random walk and for verifying that the unbiased CRW operator is recovered when the bias is removed. Let $\delta(r, \theta)$ denote the bias phase in the turning kernel, and expand

$$T(r, \theta, \phi) = \sum_{m, n \in \mathbb{Z}} U_{m, n}(r) e^{im\theta} e^{in\phi}.$$

For fixed heading mode n , the factor $e^{in\delta(r, \theta)}$ introduces spatial dependence through the polar angle θ . If $C_{n, q}(r)$ denotes its Fourier coefficients in θ , then the turning part of the BCRW

operator becomes

$$(3.6) \quad (\mathcal{L}_{\text{turn}}U)_{m,n}(r) = \mu \left[\sum_{q \in \mathbb{Z}} \frac{I_n(\kappa)}{I_0(\kappa)} C_{n,q}(r) U_{m-q,n}(r) - U_{m,n}(r) \right].$$

Thus the biased turning operator preserves the heading mode n , but mixes the position modes m through a discrete convolution. This is the Fourier-mode-space expression of the fact that the external cue introduces spatially dependent directional preference, in contrast to the unbiased CRW where the turning kernel depends only on the turning angle [1, 11, 38].

In the unbiased limit $\delta \equiv 0$, the coefficients satisfy $C_{n,0} = 1$ and $C_{n,q} = 0$ for $q \neq 0$. The convolution then collapses, and (3.6) reduces to the diagonal CRW operator in (3.4). The absorbing condition gives $U_{m,n}(a) = 0$ for all m, n , while specular reflection at the outer boundary gives

$$U_{m,n}(R) = (-1)^n U_{m+2n,-n}(R).$$

The full coupled BCRW radial system, including both streaming and turning contributions, is shown in Section C.

Boundary-layer correction to the diffusion limit MFPT. We can use the moment-closure framework for velocity-jump processes [23, 38] to identify the first correction to the diffusion-limit MFPT. Let

$$\lambda = \mu(1 - m_1), \quad m_1 = \frac{I_1(\kappa)}{I_0(\kappa)},$$

where λ is the relaxation rate of the first directional moment. We expand the CRW mean first-passage time in powers of $1/\lambda$,

$$T_{\text{CRW}}(r; \kappa) = T_0(r) + \frac{1}{\lambda} T_1(r) + \text{H.O.T.},$$

where T_0 is the leading-order (diffusion-limit) MFPT and T_1 is the first correction. At leading order the CRW reduces to a diffusion process with effective diffusivity

$$D_{\text{eff}} = \frac{s^2}{2\lambda} = \frac{s^2}{2\mu(1 - m_1)},$$

and T_0 satisfies

$$D_{\text{eff}} \Delta T_0 = -1, \quad T_0(a) = 0, \quad \partial_r T_0(R) = 0,$$

so that $T_0 = T_{\text{SRW}}^{D_{\text{eff}}}(r)$ from (3.1). The next-order term T_1 satisfies

$$D_{\text{eff}} \Delta T_1 = D_{\text{eff}}^2 \Delta^2 T_0.$$

Because $\Delta^2 T_0 = 0$ in the interior, we can see that $\Delta T_1 = 0$ inside the annulus. Specular reflection at $r = R$ is an exact transport boundary condition that is inherited order by order, giving $\partial_r T_1(R) = 0$. Together these facts imply that T_1 is constant in r and its value is not set by bulk forcing but by the kinetic boundary layer at the absorbing target, which converts the half-range absorbing condition $T(a, \psi) = 0$ for inward headings into an effective scalar

condition on the outer diffusion solution. The full calculation is given in [Section E](#) and yields

$$(3.7) \quad T_{\text{CRW}}(r; \kappa) = T_{\text{SRW}}^{D_{\text{eff}}}(r) + \mathcal{F}_{\text{abs}}(a, R, s; \kappa) + \text{H.O.T.},$$

where

$$(3.8) \quad \mathcal{F}_{\text{abs}}(a, R, s; \kappa) = \chi_{\text{abs}}(\kappa) \frac{R^2 - a^2}{as}.$$

Here $\chi_{\text{abs}}(\kappa)$ is a dimensionless extrapolation constant determined by the half-range absorbing boundary condition and the turning kernel. This form predicts that the leading finite-persistence correction shifts the radial MFPT profile by a κ -dependent constant rather than changing its radial shape, in analogy with the Milne extrapolation length that appears in mean-exit problems when a kinetic boundary layer replaces a sharp absorbing diffusion boundary condition [\[20\]](#).

4. Numerical methods.

Domain discretisation and graded mesh. We discretise the annulus using a radial grid $a = r_1 < r_2 < \dots < r_{N_r} = R$ and a uniform angular grid $\psi_j = 2\pi(j-1)/N_\psi$, $j = 1, \dots, N_\psi$. The radial nodes are placed according to a power-law, clustering toward the reflecting boundary ([Figure 2](#)),

$$(4.1) \quad r_i = a + (R - a)(1 - (1 - \xi_i)^\beta), \quad \xi_i = (i - 1)/(N_r - 1).$$

The clustering exponent β is set empirically to resolve the persistence-induced kinetic boundary layers, which narrow with κ at both the absorbing inner boundary and the reflecting outer boundary. [Subsection 5.1](#) reports the sweep that selects β and explains why a κ -dependent choice is used in the production runs.

Semi-Lagrangian (r, ψ) solver. The streaming part of [Equation \(2.3\)](#) is handled by tracing the characteristic ODEs $dr/dt = s \cos \psi$, $d\psi/dt = -s \sin \psi/r$ backward over a pseudo-time step $\Delta\tau$ to a foot-point (r_d, ψ_d) . If the trajectory crosses $r = a$ the absorbing condition $T = 0$ is enforced, and if it crosses $r = R$ the velocity is reflected $\psi \mapsto \pi - \psi$, followed by an inward nudge of $10^{-9}(R - a)$ to keep the foot point strictly inside the domain. This is followed by exact integration of the remaining time step. The interpolated value of the previous iterate at the foot-point defines $S[T^{(m)}]_{i,j}$. The turning integral is approximated by the trapezoidal rule on the uniform angular grid [\[42\]](#), and an implicit treatment of turning combined with semi-Lagrangian streaming yields the fixed-point update

$$(4.2) \quad \left(\frac{1}{\Delta\tau} + \mu\right) T_{i,j}^{(m+1)} - \mu \sum_{\ell=1}^{N_\psi} w_\ell K^*(\psi_j, \psi_\ell) T_{i,\ell}^{(m+1)} = \frac{1}{\Delta\tau} S[T^{(m)}]_{i,j} - 1.$$

At each radial level this is an $N_\psi \times N_\psi$ linear system in the angular unknowns. We iterate until the discrete residual norm $\|\mathbf{r}\|_\infty$ falls below 10^{-8} in MFPT units. The angle-averaged MFPT after convergence is computed as $\bar{T}(r_i) = (2\pi)^{-1} \sum_\ell w_\ell T_{i,\ell}$.

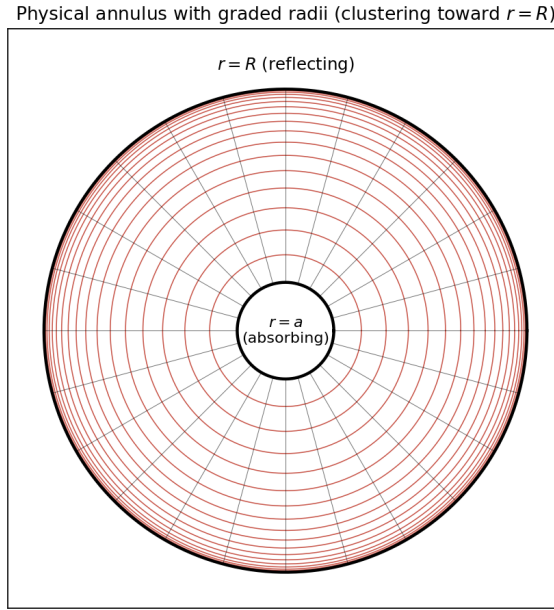


Figure 2: Power-law graded radial mesh on the annulus, shown at $\beta = 3$, $N_r = 41$, $N_\psi = 36$ for visual clarity (the production runs use larger N_r, N_ψ ; see [Subsection 5.1](#)). Radial cells cluster toward the reflecting outer boundary $r = R$ in order to resolve the persistence-induced wall layer of width $w(\kappa) \approx 5.41 \kappa^{-1.27}$, while the angular grid remains uniform. The formula gives a uniform radial mesh when $\beta = 1$.

Time step-free stationary formulation. The semi-Lagrangian iteration carries an $O(\mu\Delta\tau)$ accuracy ceiling, characterized in [Subsection 5.1](#). To remove it, we solve [Equation \(2.3\)](#) directly as a single sparse linear system. With $u_{i,j} \approx T(r_i, \psi_j)$ and an upwind treatment of the radial advection (sign of $\cos \psi_j$),

$$(4.3) \quad s \cos \psi_j (\partial_r T)_{i,j} \approx s \cos \psi_j \cdot \begin{cases} (u_{i,j} - u_{i-1,j})/h_i^- & \cos \psi_j > 0, \\ (u_{i+1,j} - u_{i,j})/h_i^+ & \cos \psi_j < 0, \end{cases}$$

combined with a centred difference for the $\partial_\psi T$ term and a boundary-aware split-Simpson rule for the angular quadrature [\[41\]](#), yields a sparse $(N_r N_\psi) \times (N_r N_\psi)$ block-banded linear system. Specular reflection at $r = R$ is enforced as a permutation block coupling ψ_j to $\pi - \psi_j$, and the absorbing condition at $r = a$ is imposed by row replacement. The system is solved in one shot by a sparse direct solver.

BCRW solver extension. The BCRW kernel [\(2.4\)](#) depends on (r, θ) through the bias phase $\phi_0(r, \theta)$, so the angular system at each spatial node is no longer translation-invariant in ψ . We keep the semi-Lagrangian streaming step from [Section 4](#) applied to the full (r, θ, ϕ) field and replace the angular turning solve by an $N_\phi \times N_\phi$ system whose matrix entries are the position-dependent samples of K^* .

As a simple representative chemotactic field we will consider radial bias toward the absorbing target, $\phi_0(r, \theta) = \theta + \pi$ (inward radial direction), so that the problem retains rotational

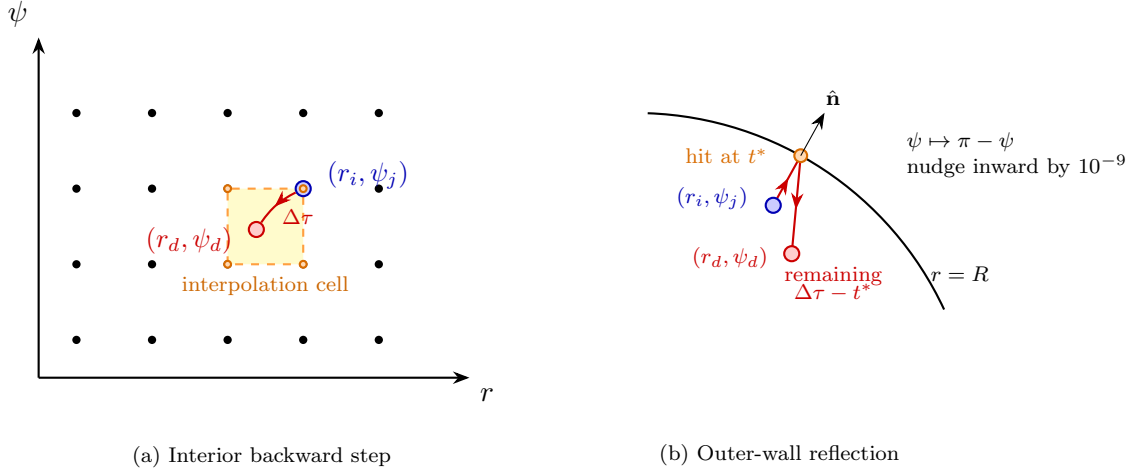


Figure 3: Semi-Lagrangian backward-characteristic step. (a) From a grid node (r_i, ψ_j) , the characteristic equation is integrated backward by $\Delta\tau$ to an off-grid foot point (r_d, ψ_d) . The value at the foot point is obtained by bilinear interpolation from the surrounding cell. (b) If the backward characteristic reaches the outer wall $r = R$ before the end of the step, the velocity is specularly reflected according to $\mathbf{v} \mapsto \mathbf{v} - 2(\mathbf{v} \cdot \hat{\mathbf{n}})\hat{\mathbf{n}}$, equivalently $\psi \mapsto \pi - \psi$, and the remaining time $\Delta\tau - t^*$ is integrated to the final foot point.

symmetry in θ and the unknown reduces to $T(r, \psi)$ with a ψ -only kernel that nonetheless breaks $\psi \rightarrow -\psi$ symmetry.

The position-dependent quadrature was verified against the unbiased CRW solver in the $d_\tau \rightarrow 0$ limit. At $d_\tau = 0$, the BCRW field reproduces the unbiased CRW field to roundoff error, confirming that the position-dependent angular system collapses to the translation-invariant CRW system in the unbiased limit. For $d_\tau > 0$ at the production grid ($\beta = 3$, $N_r = 121$, $N_\psi = 144$), the maximum probe relative deviation $|\bar{T}_{\text{BCRW}} - \bar{T}_{\text{CRW}}|/\bar{T}_{\text{CRW}}$ scales linearly in d_τ with fitted slopes 0.997 ($\kappa = 1$) and 0.990 ($\kappa = 3$), consistent with an analytical leading order expansion of the kernel. The deviation crosses the semi-Lagrangian structural ceiling of 2.7% near $d_\tau \approx 10^{-2}$ at both tested κ . We use this to set the bias range over which the BCRW solver can be compared directly with the unbiased CRW reference without being dominated by solver error. The full d_τ sweep is shown in the supplementary material (Figure 10). The unbiased limit $d_\tau = 0$ recovers Section 4. We use the small- d_τ sweep as a consistency check before reporting any chemotactic prediction.

Event-driven Monte Carlo simulation. Between turning events the walker advances ballistically along $d\mathbf{x}/dt = s(\cos\theta, \sin\theta)$, with turning events generated as a Poisson process with rate μ and new headings drawn from Equation (2.2) via the Best-Fisher rejection method [6]. Specular reflection is applied at $r = R$. From M independent realisations, $\hat{T}(r_0, \psi_0) = M^{-1} \sum_{m=1}^M \tau^{(m)}$ with the sample standard error reported as a 95% confidence interval. The event-driven simulator carries no Δt discretisation error and serves as the primary cross-validator of the deterministic solvers.

5. Verification and convergence. We verified the numerical workflow by comparing the direct (r, ψ) solver with the independent event-driven Monte Carlo simulator. Before this comparison, we checked the main building blocks of the solver separately: the discrete von Mises kernel preserves its normalization and first trigonometric moment, the absorbing boundary at $r = a$ is imposed correctly, and the specular reflection rule at $r = R$ reproduces the analytical reflected trajectory. In the semi-Lagrangian solver, the fixed-point iteration was continued until the absolute infinity-norm update satisfied $\|T^{(m+1)} - T^{(m)}\|_\infty \leq 10^{-8}$ in MFPT units. The main validation is based on the relative gap

$$g = \frac{|\bar{T}_{\text{direct}} - \hat{T}_{\text{MC}}|}{\hat{T}_{\text{MC}}},$$

reported throughout as a percentage difference $100g$ (%), where \bar{T}_{direct} is the angle-averaged direct-solver MFPT and \hat{T}_{MC} is the Monte Carlo estimate. The comparison was performed at four representative radii,

$$r \in \{1.5, 2.5, 3.5, 5\},$$

and for $\kappa \in \{0, 0.5, 1, 2, 3, 4, 5\}$.

The validation workflow is shown in [Figure 4](#), and the resulting gaps are reported in [Table 2](#) and shown in [Figure 5](#).

Our extensive validation ($M = 10^6$ MC paths per run) reveals that the semi-Lagrangian solver has a structural accuracy floor that varies with both persistence and radius r rather than a single global value. The gap is small at interior radii for $\kappa \leq 1$ ($\lesssim 1.5\%$) and grows toward the outer wall at every κ , reaching 5.0% at $(\kappa, r) = (2, 5)$ and 6.5% at $(\kappa, r) = (5, 5)$ on the production grid [\(4.1\)](#).

5.1. Outer-wall layer and calibration of the graded mesh. The semi-Lagrangian solver has two kinetic boundary layers whose width narrows with κ : one at the absorbing inner boundary $r = a$ and one at the reflecting outer boundary $r = R$ (persistence-induced wall layer). A fit to the layer width and amplitude on uniform grids gives

$$(5.1) \quad w(\kappa) \approx 5.41 \kappa^{-1.27}, \quad A(\kappa) \approx 2.95 \kappa^{0.835},$$

over $\kappa \in \{0.5, 1, 2, 5, 10\}$. The layer narrows and strengthens with persistence, so the chosen mesh must be both κ -dependent and graded.

The adaptive mesh reduces to a uniform radial mesh at $\beta = 1$ and concentrates resolution at $r = R$ as β grows. A sweep over $\beta \in \{1.5, 2, 3, 5\}$ and $N_r \in \{91, 121, 181, 241, 361, 541\}$ at $N_\psi = 144$, $\Delta\tau = 0.007$ identified the candidate production grid [\(4.1\)](#). The low- κ branch uses a gentle grading ($\beta = 1.5$) with a refined radial grid ($N_r = 361$) to resolve the inner Milne layer that dominates at low persistence, while the high- κ branch uses strong outer clustering ($\beta = 3$) at a moderate radial count ($N_r = 241$) to resolve the narrowing outer wall layer. Comparison against extensive Monte Carlo simulation ($M = 10^6$ runs) on this grid is reported in [Table 2](#). The residual SL-vs-MC gap reflects the $O(\mu\Delta\tau)$ structural ceiling of the pseudo-time formulation rather than unresolved layer structure, and is removed in the stationary solver.

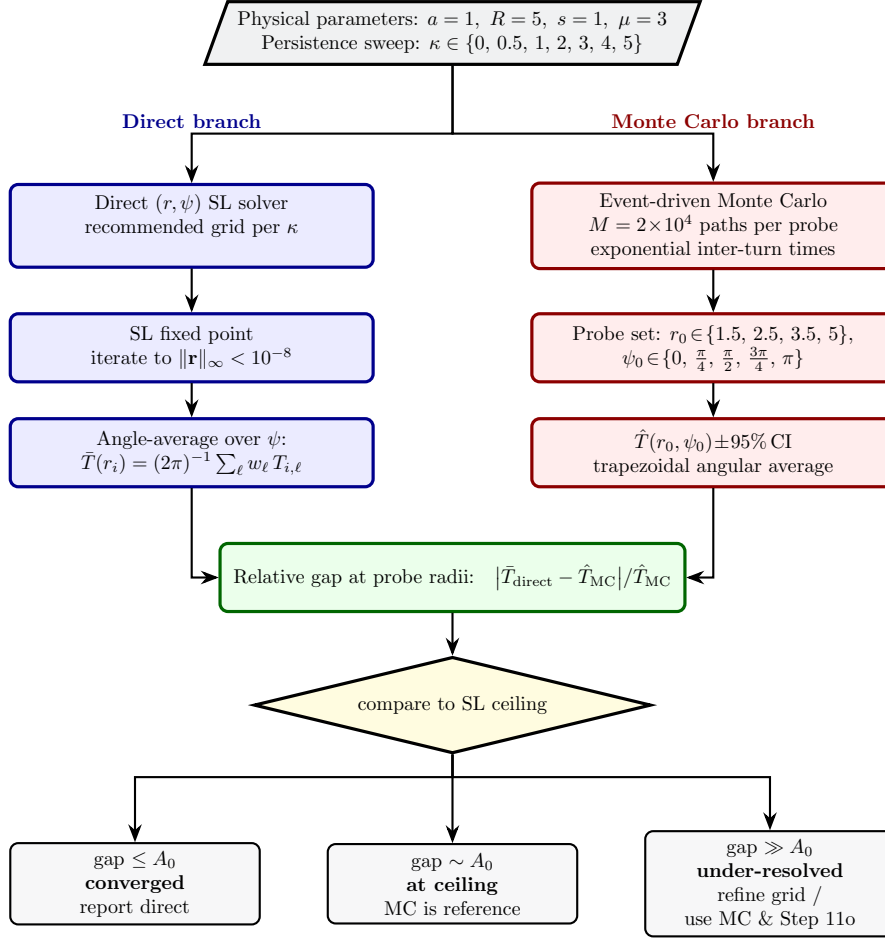


Figure 4: Validation workflow. The direct (r, ψ) solver and the event-driven Monte Carlo simulator are run independently at the same parameter values. Their angle-averaged MFPTs are compared using the relative gap. Small gaps indicate convergence, gaps near the observed semi-Lagrangian ceiling indicate the limitation of the pseudo-time formulation, and larger gaps indicate under resolution or transition to the strong persistence regime.

6. Biological calibration and predictions.

6.1. Mapping the concentration parameter to cell migration data. To connect the numerical persistence sweep to biological motility data, we use the one-step directional persistence

$$c = \langle \cos \Delta\theta \rangle = \frac{I_1(\kappa)}{I_0(\kappa)}.$$

This mapping is monotone: $c = 0$ corresponds to isotropic reorientation, while $c \rightarrow 1$ corresponds to highly persistent motion. Representative cell-tracking studies place many biological

Table 2: Direct-vs-Monte-Carlo percentage difference $100 |\bar{T}_{\text{direct}} - \widehat{T}_{\text{MC}}| / \widehat{T}_{\text{MC}}$. The gap defines the (κ, r) -dependent semi-Lagrangian structural floor. Largest values appear at the reflecting outer boundary ($r = 5$) for $\kappa \geq 2$ and at the absorbing inner probe ($r = 1.5$) for $\kappa \geq 3$, reflecting the two kinetic boundary layers. Values are given to two decimal places.

κ	probe radius r			
	1.5	2.5	3.5	5
0	0.82	0.39	0.08	0.35
0.5	0.75	0.23	0.69	1.38
1	0.29	1.35	1.41	2.65
2	1.12	2.13	2.49	5.01
3	4.05	2.23	2.13	2.21
4	4.16	2.43	2.17	4.42
5	4.17	2.55	2.33	6.55

Table 3: Approximate mapping between representative biological motility classes and the von Mises persistence parameter. Values are approximate because the underlying studies use different sampling intervals, imaging environments, and motility summaries.

Cell class	c	κ	Source
<i>E. coli</i> run-and-tumble	≈ 0.3	≈ 0.7	[5, 4]
T cells / lymphocytes in tissue	0.4–0.7	0.9–2	[36, 37, 3]
NK cells in lymph node	0.4–0.7	0.9–2	[2]
Neutrophils, monocytes in 2D	0.5–0.8	1–3	[27]
Fibroblasts, mesenchymal cells	0.7–0.9	2–5	[14, 34]
<i>Dictyostelium</i> in vitro	0.85–0.95	3–10	[43]
Keratocytes	$\gtrsim 0.95$	$\gtrsim 10$	[13, 32, 28]

walkers in the range

$$c \approx 0.3\text{--}0.9, \quad \kappa \approx 0.7\text{--}5.$$

This includes run-and-tumble *E. coli*, lymphocytes and NK-cell-like motion in lymph nodes, neutrophils, monocytes, fibroblasts, and other mesenchymal cells [2, 3, 4, 5, 14, 27, 34, 36, 37]. More strongly persistent cells, such as *Dictyostelium* and keratocytes, can extend beyond this range and motivate the strong persistence discussion in Subsection 3.1 [13, 28, 32, 43] and in the ecological random walk literature [10, 11]. We therefore take

$$\kappa \in (0, 5]$$

as the main biologically relevant and numerically validated range for the present study.

6.2. T-cell prediction: search-time reduction and diminishing returns. We next evaluate the model using parameters representative of T-cell motion in intact lymph node. We use

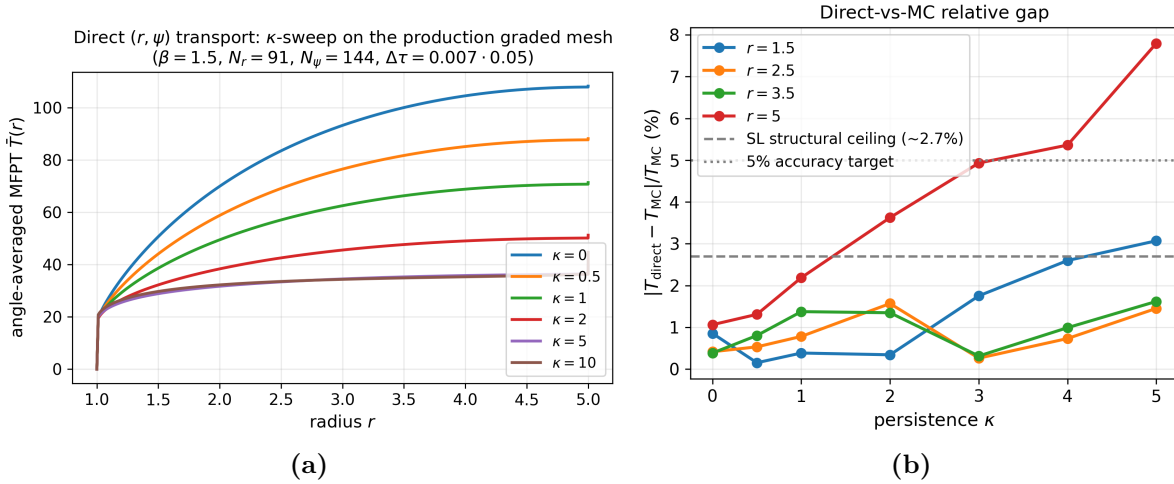


Figure 5: Persistence sweep and validation of the direct semi-Lagrangian solver in the annulus $a < r < R$ with absorbing inner boundary at $r = a$ and specularly reflecting outer boundary at $r = R$. Parameters: $a = 1, R = 5$, walker speed $s = 1$, turning rate $\mu = 3$. Grid: graded mesh with clustering exponent β and radial/angular node counts (N_r, N_ψ) chosen per κ following (4.1); pseudo-time step $\Delta\tau \in [0.007, 0.05]$. (a) Angle-averaged MFPT profiles from the direct (r, ψ) transport solver across the persistence sweep $\kappa \in \{0, 0.5, 1, 2, 3, 4, 5\}$. Increasing κ decreases the MFPT over the validated range $\kappa \in [0, 5]$. The $\kappa = 10$ curve is shown only to illustrate the onset of the high-persistence regime, where the semi-Lagrangian solver is no longer used as the primary reference. (b) Direct-vs-Monte-Carlo percentage difference $100|\bar{T}_{\text{direct}} - \hat{T}_{\text{MC}}|/\hat{T}_{\text{MC}}$ at the four probe radii $r_0 \in \{1.5, 2.5, 3.5, 5\}$, evaluated against the event-driven Monte Carlo reference ($M = 2 \times 10^4$ paths per probe; see Section 4). The dashed line marks the representative Richardson-extrapolated ceiling $A_0 \approx 2.7\%$ at $(\kappa, r) = (5, 5)$, shown for reference. The largest gaps occur near the reflecting wall at $r = 5$ for $\kappa \geq 2$ and additionally at the absorbing inner probe $r = 1.5$ for $\kappa \geq 3$, reflecting the kinetic boundary layers at the two boundaries.

speed $s = 11 \mu\text{m}/\text{min}$ [37], turning rate $\mu = 0.5 \text{ min}^{-1}$ from persistence time $\tau_p \approx 2 \text{ min}$ [3], target radius $a = 10 \mu\text{m}$ (an antigen-presenting dendritic cell with extended dendritic processes) [33], and paracortex radius $R = 200 \mu\text{m}$ [3]. The purpose of this calculation is not to reproduce a specific experiment, but to translate the mathematical persistence parameter into a biologically interpretable search time prediction. Table 4 reports the angle-averaged MFPT at three representative starting radii, $r_a = 20 \mu\text{m}$, $r_b = 100 \mu\text{m}$, and $r_0 = R = 200 \mu\text{m}$, for $\kappa \in \{0, 1, 1.5, 2, 3, 5\}$. The row $\kappa = 0$ gives the isotropic reorientation baseline, while $\kappa \approx 1-2$ represents the typical lymphocyte range. Increasing κ reduces the search time relative to the baseline, with most of the improvement concentrated in $\kappa \in [0, 2]$ and the reduction per unit κ falling below 10% of the $\kappa = 0 \rightarrow 1$ baseline only at $\kappa = 5$. The MFPT therefore continues to decrease across the validated range, with progressively diminishing additional benefit.

Table 4: T cell MFPT prediction across persistence at three starting radii, from event-driven Monte Carlo simulation ($M = 10^6$ paths per cell, $\pm 95\%$ CI shown in parentheses). Biological parameters: speed $s = 11 \mu\text{m}/\text{min}$ [37], turning rate $\mu = 0.5 \text{ min}^{-1}$ from persistence time $\tau_p \approx 2 \text{ min}$ [3], target radius $a = 10 \mu\text{m}$ [33], paracortex radius $R = 200 \mu\text{m}$ [3]. Starting radii are $r_a = 20 \mu\text{m}$ (near-target probe), $r_b = 100 \mu\text{m}$ (mid-paracortex probe), and $r_0 = R = 200 \mu\text{m}$ (outer-paracortex probe). MFPT values are in minutes.

κ	$\bar{T}(r_0 = 20 \mu\text{m})$	$\bar{T}(r_0 = 100 \mu\text{m})$	$\bar{T}(r_0 = 200 \mu\text{m})$
0	548.9 (± 1.6)	800.2 (± 1.7)	854.3 (± 1.7)
1	504.2 (± 1.3)	650.2 (± 1.4)	679.9 (± 1.4)
1.5	493.9 (± 1.2)	604.2 (± 1.3)	626.8 (± 1.3)
2	488.7 (± 1.2)	576.9 (± 1.2)	595.1 (± 1.2)
3	485.7 (± 1.1)	554.4 (± 1.1)	566.3 (± 1.1)
5	488.1 (± 1.1)	545.4 (± 1.1)	556.0 (± 1.1)

Table 5: Applicability of the diffusion limit and boundary-layer correction at T-cell parameters. The Milne extrapolation length $\ell_{\text{abs}}(\kappa) = s/\lambda(\kappa)$ with $\lambda(\kappa) = \mu(1 - m_1(\kappa))$ is not small compared with the annulus width $R - a = 190 \mu\text{m}$ at any κ , so the boundary-layer correction does not apply in this parameter regime.

κ	$\lambda \text{ (min}^{-1}\text{)}$	$\ell_{\text{abs}} \text{ (}\mu\text{m)}$	$\ell_{\text{abs}}/(R - a)$
0	0.500	22.0	0.116
1	0.277	39.7	0.209
1.5	0.202	54.5	0.287
2	0.151	72.8	0.383
3	0.095	115.8	0.609
5	0.053	206.3	1.086

The diffusion-limit baseline lies far below the Monte Carlo MFPT at all κ (Figure 8). The diffusion approximation predicts $\sim 115 \text{ min}$ at r_a for $\kappa = 0$, while the kinetic MFPT is $\sim 549 \text{ min}$, a factor of ~ 5 underestimate. This gap is not a numerical artefact but a consequence of the parameter regime: with $s/\mu = 22 \mu\text{m}$ comparable to the inner geometry $a = 10 \mu\text{m}$, the walker frequently turns less than once before reaching the target from the inner start point, and the fast-turning assumption underlying the diffusion limit does not hold. The boundary layer correction does not apply either since the extrapolation length $\ell_{\text{abs}}(\kappa) \sim s/\lambda(\kappa)$ exceeds 10% of the annulus width $R - a$ already at $\kappa = 0$ and grows with persistence (Table 5). The kinetic transport framework developed in this paper is therefore not a refinement to the diffusion limit at T-cell parameters. Rather, it provides the leading-order prediction itself.

7. Main result. The main conclusion of this study is that directional persistence reduces the mean search time in the annular target problem, but the benefit saturates once persistence is sufficiently large. More precisely, for a correlated random walk in the annulus $a < r < R$,

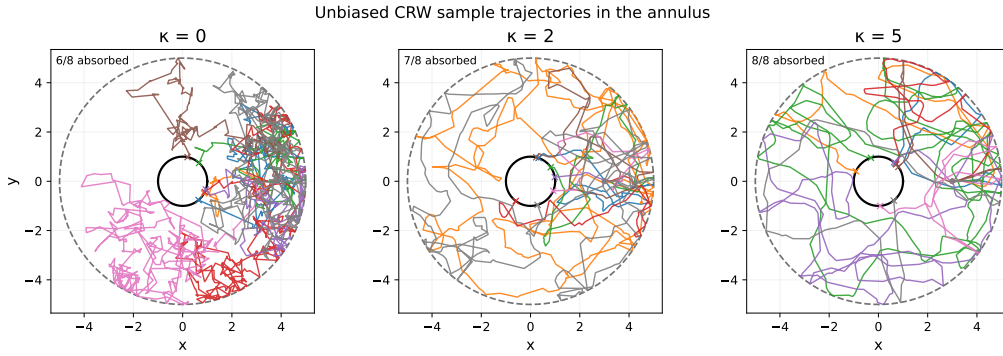


Figure 6: Representative CRW trajectories in the annulus at three persistence levels. Increasing κ produces longer straight runs between turns, reduces redundant coverage, and increases the fraction absorbed within the cutoff (shown in each panel).

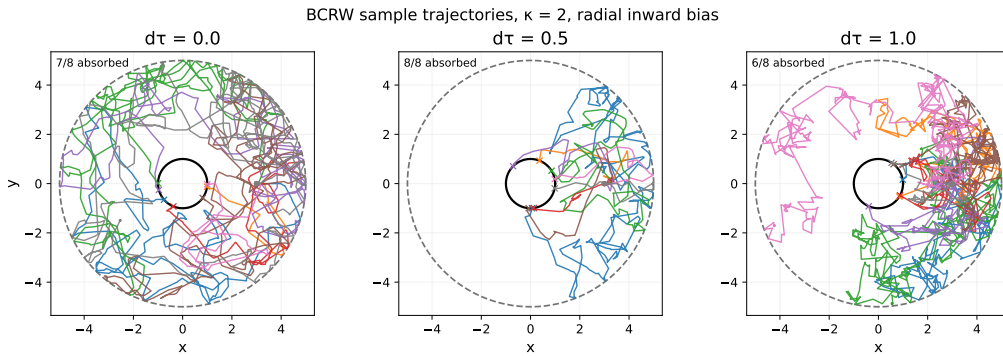


Figure 7: Representative BCRW trajectories at $\kappa = 2$ for three bias strengths. Increasing time step length draws paths toward the absorbing target, reducing the exploratory wandering visible at and increasing the absorbed fraction within the cutoff.

with absorbing inner boundary at $r = a$, specular reflection at $r = R$, constant speed s , turning rate μ , and von Mises turning kernel with concentration κ , the angle-averaged mean first-passage time $\bar{T}(r_0; \kappa)$ decreases with κ over the validated range $\kappa \in [0, 5]$. This trend holds at all tested starting radii $r_0 \in (a, R]$, and the reduction becomes weaker near $\kappa \approx 5$.

This result is supported by several independent calculations. In the fast-turning limit, the correlated random walk reduces to diffusion with effective diffusivity

$$D_{\text{eff}} = \frac{s^2}{2\mu(1 - m_1(\kappa))}, \quad m_1(\kappa) = \frac{I_1(\kappa)}{I_0(\kappa)}.$$

Since $m_1(\kappa)$ increases with κ , the effective diffusivity also increases with κ . The diffusion-limit MFPT therefore decreases as persistence increases. The absorbing-boundary correction derived in [Section E](#) preserves this interpretation: finite persistence shifts the MFPT by a boundary-layer offset rather than changing the leading radial dependence in the bulk.

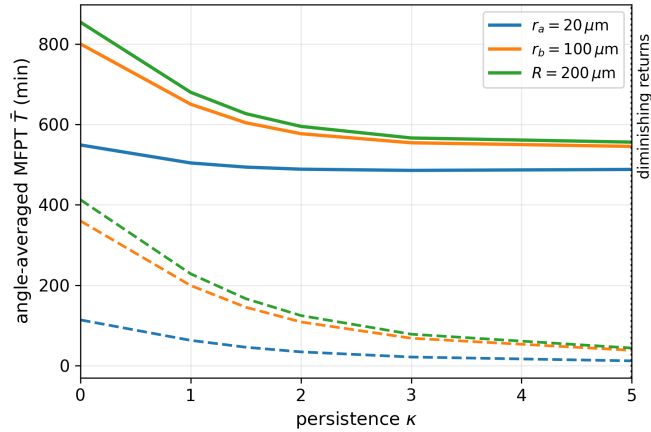


Figure 8: T-cell angle-averaged MFPT $\bar{T}(r_0; \kappa)$ versus persistence parameter κ at three starting radii, from event-driven Monte Carlo ($M = 10^6$ paths per cell; solid curves, \pm CI95 narrower than line width). Dashed curves: diffusion-limit baseline $T_{\text{SRW}}^{D_{\text{eff}}}$ with $D_{\text{eff}} = s^2/(2\mu(1 - m_1(\kappa)))$, shown for reference. The diffusion limit underestimates the kinetic MFPT by a factor of ~ 4 – 5 at low κ because the mean free path $s/\mu = 22 \mu\text{m}$ is comparable to the inner geometry $a = 10 \mu\text{m}$ and the diffusion approximation does not apply. The boundary layer correction is omitted because $\ell_{\text{abs}}(\kappa)/(R - a)$ is not small at any tested κ (Table 5). The vertical dotted line marks the diminishing-returns threshold $\kappa^* = 5$, at which the marginal reduction in search time per unit κ first falls below 10% of the $\kappa = 0 \rightarrow 1$ baseline.

The numerical results support the same conclusion beyond the diffusion limit. The diffusion approximation accounts for the leading behaviour at moderate persistence, but as κ grows the walker enters the strong-persistence regime described in the last part of Section 3: the von Mises kernel concentrates near zero turning angle, the angular turning operator is approximated by angular diffusion with $D_\psi = \mu/\kappa$, and the radial motion becomes nearly deterministic between rare changes in heading. In this limit the MFPT approaches the ballistic-hitting time set by the chord geometry of the annulus rather than the diffusion-limit MFPT, so $\bar{T}(r_0; \kappa)$ continues to decrease with κ but with diminishing additional benefit. The two analytical limits therefore bound the validated range from below and above, both predicting a monotone reduction in search time with persistence.

The semi-Lagrangian (r, ψ) solver reproduces this monotone decrease of $\bar{T}(r_0; \kappa)$ at all probe radii $r_0 \in \{1.5, 2.5, 3.5, 5\}$ over the validated range $\kappa \in [0, 5]$. The event-driven Monte Carlo simulator gives an independent check of the same trend, including the high-persistence comparison at $r = 5$. The time step-free stationary formulation further confirms the trend at $\kappa = 5$ without the structural accuracy ceiling associated with the pseudo-time semi-Lagrangian formulation. Together, these analytical, deterministic numerical, and Monte Carlo results show that persistence accelerates confined target search over the biologically relevant range, with diminishing additional benefit as the motion approaches the strong-persistence regime.

8. Discussion. The monotone reduction of search time with increasing persistence is consistent with the broader random-walk literature in biology and ecology, where directional persistence often reduces encounter times by allowing a walker to explore space more efficiently [11, 10]. The contribution of the present work is to quantify this effect for a confined annular search geometry with an absorbing central target and a specularly reflecting outer boundary. In this setting, persistence improves search efficiency over the biologically relevant range $\kappa \in [0, 5]$, but the improvement begins to saturate near the upper end of this range.

The analysis also clarifies how the correlated random walk connects to simpler diffusion-based models. In the fast-turning regime, persistence enters through the effective diffusivity D_{eff} , giving a direct analytical explanation for why increasing κ reduces the MFPT. The next correction is not a smooth r -dependent bulk correction in the annulus. Instead, the leading finite-persistence effect appears as an absorbing-boundary, Milne-type offset. This provides a simple way to estimate the deviation from the diffusion-limit prediction without solving the full transport problem.

The numerical workflow separates the regimes in which different approximations are reliable. For $\kappa \in [0, 5]$, the semi-Lagrangian solver, the stationary formulation, and Monte Carlo simulations give consistent trends. For larger κ , the motion enters a strong-persistence regime in which the near-wall layer becomes difficult to resolve on accessible semi-Lagrangian grids. In that regime, Monte Carlo and the strong-persistence analysis become the more reliable references. This is also the regime relevant to highly persistent cells such as keratocytes and some *Dictyostelium* conditions.

Several limitations remain. The present model is restricted to a two-dimensional, rotationally symmetric annulus with a single absorbing target at the center. It does not include three-dimensional tissue geometry, multiple targets, asymmetric confinement, cell-cell interactions, spatially varying speeds, or Lévy-walk behavior [21]. The biased correlated random walk formulation developed here also remains to be completed numerically for nontrivial chemotactic fields.

Natural extensions include applying the time step-free stationary formulation as the main production solver, completing the BCRW solver for spatially varying guidance cues, extending the boundary-layer correction beyond leading order, and moving from the annulus to three-dimensional spheroid and more complex multi-target geometries. The recent higher-dimensional velocity-jump MFPT framework of [12], which develops a Langevin approximation and explicit MFPT formulae for von Mises and Fisher kernels in $d = 2, 3$, provides a natural template for the three-dimensional extension and for incorporating chemotactic bias through a spatially varying preferred direction.

Appendix A. Finite-difference benchmarks for SRW and BRW. This appendix explains the second order centered finite difference solver used to verify the analytical hierarchy of [Subsection 3.1](#). The radial interval $[a, R]$ is discretized uniformly with $h = (R-a)/(N_r-1)$. At each interior node the differential operator is replaced by its centered difference approximation, and the reflecting outer boundary by the second order backward difference $3u_{N_r-1} - 4u_{N_r-2} + u_{N_r-3} = 0$.

[Table 6](#) reports the constant diffusivity SRW grid convergence study at $a = 1$, $R = 5$, $D = 1$; the observed order approaches 2. The observed second-order convergence confirms the finite-difference implementation; the same scheme is applied without modification to the variable-coefficient SRW and BRW cases used as simulations in [Section 3](#).

Table 6: Constant-diffusivity SRW grid-convergence study, $a = 1$, $R = 5$, $D = 1$.

N_r	h	$\max_i u_{\text{num}} - u_{\text{exact}} $	max rel. err	order
50	8.16×10^{-2}	8.99×10^{-4}	3.20×10^{-4}	–
100	4.04×10^{-2}	2.26×10^{-4}	8.45×10^{-5}	1.96
200	2.01×10^{-2}	5.66×10^{-5}	2.17×10^{-5}	1.98
400	1.00×10^{-2}	1.42×10^{-5}	5.49×10^{-6}	1.99

Appendix B. Specular reflection at the outer boundary. This appendix explains the derivation of the specular reflection condition and places it in the general framework of kinetic boundary conditions for transport equations.

At the outer wall the local frame is $\vec{e}_r(\theta) = (\cos \theta, \sin \theta)$, $\vec{e}_\theta(\theta) = (-\sin \theta, \cos \theta)$. The incoming velocity $\vec{V}_{\text{old}} = s(\cos \phi, \sin \phi)$ projects onto this frame as

$$(B.1) \quad v_r = \vec{V}_{\text{old}} \cdot \vec{e}_r = s \cos(\phi - \theta), \quad v_\theta = \vec{V}_{\text{old}} \cdot \vec{e}_\theta = s \sin(\phi - \theta),$$

so that $\vec{V}_{\text{old}} = s \cos(\phi - \theta) \vec{e}_r + s \sin(\phi - \theta) \vec{e}_\theta$. Specular reflection flips the radial component and preserves the tangential component,

$$(B.2) \quad \vec{V}_{\text{new}} = -v_r \vec{e}_r + v_\theta \vec{e}_\theta = -s \cos(\phi - \theta) \vec{e}_r + s \sin(\phi - \theta) \vec{e}_\theta.$$

Writing this in angle space, with ϕ' the incoming direction and ϕ the reflected direction, $\phi' - \theta \mapsto \pi - (\phi - \theta)$, so that

$$(B.3) \quad \phi(\theta, \phi') = 2\theta + \pi - \phi'.$$

In the heading variable $\psi = \phi - \theta$, which is the natural variable for the rotationally symmetric unbiased problem, [Equation \(B.3\)](#) reduces to the CRW boundary condition

$$(B.4) \quad T(R, \psi) = T(R, \pi - \psi).$$

For the BCRW, the same identity [\(2.7\)](#) is kept in the general form. Schematics is shown in [Figure 9](#).

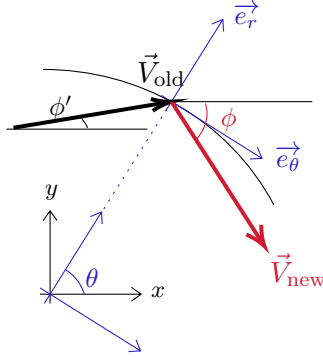


Figure 9: Specular reflection in the local frame at the outer boundary $r = R$.

Appendix C. BCRW Fourier hierarchy.

This appendix focuses on the full mode-space form of the biased correlated random walk (BCRW) backward equation (2.5). We expand the MFPT in the two angular variables as

$$T(r, \theta, \phi) = \sum_{m, n \in \mathbb{Z}} U_{m, n}(r) e^{im\theta} e^{in\phi}.$$

in the streaming terms, then couple neighboring angular modes. In particular,

$$(C.1) \quad [\cos(\phi - \theta) \partial_r T]_{m, n} = \frac{1}{2} (U'_{m+1, n-1}(r) + U'_{m-1, n+1}(r)),$$

$$(C.2) \quad \left[\frac{\sin(\phi - \theta)}{r} \partial_\theta T \right]_{m, n} = \frac{1}{2r} ((m+1)U_{m+1, n-1}(r) - (m-1)U_{m-1, n+1}(r)).$$

Combining these identities with the Fourier representation of the turning operator in (3.6), and matching coefficients of $e^{im\theta} e^{in\phi}$, gives the coupled radial hierarchy

$$(C.3) \quad -\delta_{m,0} \delta_{n,0} = \frac{s}{2} (U'_{m+1, n-1} + U'_{m-1, n+1}) + \frac{s}{2r} ((m+1)U_{m+1, n-1} - (m-1)U_{m-1, n+1}) \\ + \mu \left[\sum_{q \in \mathbb{Z}} \frac{I_n(\kappa)}{I_0(\kappa)} C_{n, q} U_{m-q, n}(r) - U_{m, n}(r) \right].$$

The absorbing boundary condition gives

$$U_{m, n}(a) = 0 \quad \text{for all } m, n,$$

while specular reflection at the outer boundary gives

$$U_{m, n}(R) = (-1)^n U_{m+2n, -n}(R).$$

Here $C_{n, q}$ denotes the q th Fourier coefficient, in the variable θ , of $e^{in\delta(r, \theta)}$, where $\delta(r, \theta)$ is the phase shift associated with the bias direction. Thus the biased turning operator is no longer

diagonal in the position mode m ; instead, the spatial dependence of the bias introduces a convolution over m .

In the unbiased limit $\delta \equiv 0$, the coefficients satisfy

$$C_{n,0} = 1, \quad C_{n,q} = 0 \quad \text{for } q \neq 0.$$

The convolution then collapses, and the turning operator reduces to the diagonal CRW operator in (3.4). This recovers the unbiased CRW hierarchy (3.5).

Appendix D. Compatibility issues in truncated mode-space formulations.

Before adopting the direct (r, ψ) transport solver described in Section 4, we tested a family of truncated-Fourier formulations for Equation (2.3). These formulations are recorded here to clarify why they were not used as the main numerical method.

After Fourier reduction and truncation, the resulting radial system can be written in the form

$$Mw'(r) + B(r)w(r) = f,$$

where the matrix M is singular. Consequently, any left-null vector ℓ of M imposes an algebraic compatibility condition,

$$\ell^\top B(r)w(r) = \ell^\top f.$$

In practice, this compatibility condition was not simultaneously consistent with the absorbing boundary data and the finite-mode truncation, even in the lowest nontrivial truncation. We observed the same issue across several variants, including buffered differential algebraic systems, retained mode reductions with $N = 1$ and $N = 2$, asymptotic closures for omitted modes, and finite- K non-buffered spectral reference systems.

In each case, the transformed discrete system could be solved to high numerical accuracy, but the residual in the original physical transport equation did not decrease under refinement, and in some cases increased. Block elimination, Schur-complement methods, direct solvers, and QR-based consistency solvers all led to the same physical residual behavior. This indicates that the main issue is the finite-mode formulation itself rather than the choice of linear algebra solver. For this reason, the mode-space systems are used only as analytical and diagnostic tools in the present work, while the primary computations are based on the direct stationary transport discretization.

Appendix E. Boundary-layer correction in the annulus.

We summarize the calculation leading to the absorbing-boundary correction used in Subsection 3.1. Let

$$\lambda = \mu(1 - m_1), \quad m_1 = \frac{I_1(\kappa)}{I_0(\kappa)}, \quad D_{\text{eff}} = \frac{s^2}{2\lambda}.$$

The leading outer solution is the diffusion-limit MFPT

$$D_{\text{eff}}\Delta T_0 = -1, \quad T_0(a) = 0, \quad \partial_r T_0(R) = 0,$$

and therefore

$$(E.1) \quad T_0(r) = \frac{R^2}{2D_{\text{eff}}} \log \frac{r}{a} + \frac{a^2 - r^2}{4D_{\text{eff}}}.$$

We write the transport MFPT as

$$T_{\text{CRW}}(r; \kappa) = T_0(r) + \frac{1}{\lambda} T_1(r) + \dots$$

The Chapman–Enskog correction to the bulk equation [23, 38] gives

$$D_{\text{eff}} \Delta T_1 = D_{\text{eff}}^2 \Delta^2 T_0.$$

Since $D_{\text{eff}} \Delta T_0 = -1$ in the annulus, $\Delta^2 T_0 = 0$, and hence

$$\Delta T_1 = 0.$$

For a radial correction this gives

$$T_1(r) = A \log r + B.$$

The outer boundary is specularly reflecting, so no absorbing kinetic layer is generated at $r = R$, and the outer expansion inherits the reflecting condition order by order:

$$\partial_r T_1(R) = 0.$$

Thus $A = 0$, and the first regular correction is a constant independent of the starting radius.

The value of this constant is set by the absorbing boundary layer at $r = a$. The transport condition is a half-range condition, imposed only on headings entering the target, rather than the scalar diffusion condition $T(a) = 0$. In the outer diffusion problem this is replaced by the Milne-type extrapolation condition

$$T_{\text{out}}(a) = \ell_{\text{abs}} \partial_r T_{\text{out}}(a), \quad \ell_{\text{abs}} = \chi_{\text{abs}}(\kappa) \frac{s}{\lambda},$$

where $\chi_{\text{abs}}(\kappa)$ is the dimensionless half-space extrapolation constant for the von Mises turning kernel.

At this order $T_{\text{out}} = T_0 + B$, and since $T_0(a) = 0$,

$$B = \ell_{\text{abs}} T_0'(a).$$

Using

$$T_0'(a) = \frac{R^2 - a^2}{2D_{\text{eff}}a}, \quad D_{\text{eff}} = \frac{s^2}{2\lambda},$$

we obtain

$$B = \chi_{\text{abs}}(\kappa) \frac{R^2 - a^2}{as}.$$

Therefore

$$(E.2) \quad T_{\text{CRW}}(r; \kappa) = T_{\text{SRW}}^{D_{\text{eff}}}(r) + \chi_{\text{abs}}(\kappa) \frac{R^2 - a^2}{as} + \text{higher-order terms}.$$

The correction is independent of r because the regular interior correction has a zero Laplacian and the reflecting boundary removes the logarithmic mode. Its magnitude is set by the absorbing kinetic layer through $\chi_{\text{abs}}(\kappa)$.

The constant $\chi_{\text{abs}}(\kappa)$ is a Milne-type extrapolation constant: it is the dimensionless constant obtained by solving the half-space kinetic boundary-layer problem associated with the half-range absorbing boundary condition. Such extrapolation constants are standard in diffusion-limit analyses of kinetic and transport equations, where the kinetic boundary layer converts a microscopic inflow or absorbing boundary condition into an effective boundary condition for the outer diffusion problem [8, 29, 19].

This result also gives two useful consistency checks. When $\kappa = 0$, the kernel is isotropic and $\lambda = \mu$. The extrapolation constant $\chi_{\text{abs}}(0)$ is finite, so the calculation predicts a nonzero offset between the diffusion-limit SRW formula and the full velocity-jump MFPT even for isotropic reorientation. This offset is not a solver error; it is the absorbing-wall kinetic correction. In contrast, as $\kappa \rightarrow \infty$, $m_1 \rightarrow 1$, so $\lambda \rightarrow 0$ and the extrapolation length s/λ becomes large. The Milne layer is then no longer thin relative to the annulus, and the diffusion expansion breaks down. This is the strong persistence regime treated separately in the numerical verification.

Acknowledgments. We thank Thomas Hillen, Alan Lindsay, Sarafa Iyaniwura and especially Michael Ward for helpful discussions during the development of this project.

Author Contributions. FS: Problem development; model set-up; analytical work and approximations; numerical methods and testing; writing the manuscript. DC: Problem development; analytical work and approximations; writing the manuscript.

Access to Code. At present, please send requests for code to the authors.

REFERENCES

- [1] W. ALT, *Biased random walk models for chemotaxis and related diffusion approximations*, Journal of Mathematical Biology, 9 (1980), pp. 147–177, <https://doi.org/10.1007/BF00275919>.
- [2] M. BAJÉNOFF, B. BREART, AND R. N. GERMAIN, *Natural killer cell behavior in lymph nodes revealed by static and real-time imaging*, J. Exp. Med., 203 (2006), pp. 619–631.
- [3] J. B. BELTMAN ET AL., *Lymph node topology dictates T cell migration behavior*, J. Exp. Med., 204 (2007), pp. 771–780.
- [4] H. C. BERG, *E. coli in Motion*, Springer, 2004.
- [5] H. C. BERG AND D. A. BROWN, *Chemotaxis in Escherichia Coli analysed by three-dimensional tracking*, Nature, 239 (1972), pp. 500–504.
- [6] D. J. BEST AND N. I. FISHER, *Efficient simulation of the von Mises distribution*, Appl. Stat., 28 (1979), pp. 152–157.
- [7] P. BRESSLOFF AND J. NEWBY, *Quasi-steady state analysis of motor-driven transport on a two-dimensional microtubular network*, Phys. Rev. E, 83 (2011), p. 061139.
- [8] C. CERCIGNANI, *Mathematical Methods in Kinetic Theory*, Plenum Press, New York, 1969.
- [9] A. CHEVIAKOV AND M. WARD, *Optimization of trap locations for narrow capture problems*, in Target Search Problems, Springer, 2024, pp. 225–246.
- [10] E. A. CODLING, *Biased Random Walks in Biology*, PhD thesis, University of Leeds, Leeds, UK, 2003.
- [11] E. A. CODLING, M. J. PLANK, AND S. BENHAMOU, *Random walk models in biology*, Journal of the Royal Society Interface, 5 (2008), pp. 813–834, <https://doi.org/10.1098/rsif.2008.0014>.
- [12] M. R. D’ORSOGNA, A. E. LINDSAY, AND T. HILLEN, *Mean first passage times of higher-dimensional velocity jump processes*, arXiv preprint arXiv:2603.29241, (2026).

- [13] U. EUTENEUER AND M. SCHLIWA, *Persistent, directional motility of fish keratocytes in vitro*, *Nature*, 310 (1984), pp. 58–61.
- [14] M. H. GAIL AND C. W. BOONE, *The locomotion of mouse fibroblasts in tissue culture*, *Biophys. J.*, 10 (1970), pp. 980–993.
- [15] D. S. GREBENKOV, *Full distribution of first exit times in the narrow escape problem*, *New Journal of Physics*, 21 (2019), p. 122001, <https://doi.org/10.1088/1367-2630/ab5de4>.
- [16] D. S. GREBENKOV, R. METZLER, AND G. OSHANIN, *From single-particle stochastic kinetics to macroscopic reaction rates: Fastest first-passage time of N random walkers*, *New Journal of Physics*, 22 (2020), p. 103004, <https://doi.org/10.1088/1367-2630/abb1de>.
- [17] D. S. GREBENKOV, R. METZLER, AND G. OSHANIN, eds., *Target Search Problems*, Springer, Cham, 2024, <https://doi.org/10.1007/978-3-031-67802-8>.
- [18] D. S. GREBENKOV AND M. J. WARD, *Competition of small targets in planar domains: from Dirichlet to Robin and Steklov boundary condition*, *European Journal of Applied Mathematics*, (2026).
- [19] Y. GUO, *l^2 diffusive expansion for neutron transport equation*, *Communications on Applied Mathematics*, 5 (2025), pp. 101–119, <https://doi.org/10.3934/cam.2025015>.
- [20] P. S. HAGAN, C. R. DOERING, AND C. D. LEVERMORE, *Mean exit times for particles driven by weakly colored noise*, *SIAM Journal on Applied Mathematics*, 49 (1989), pp. 1480–1513, <https://doi.org/10.1137/0149090>.
- [21] T. H. HARRIS ET AL., *Generalized Lévy walks and the role of chemokines in migration of effector CD8+ T cells*, *Nature*, 486 (2012), pp. 545–548.
- [22] T. HILLEN, M. R. D’ORSOGNA, J. C. MANTOOTH, AND A. E. LINDSAY, *Mean first passage times for transport equations*, *SIAM Journal on Applied Mathematics*, 85 (2025), pp. 78–108.
- [23] T. HILLEN AND H. G. OTHMER, *The diffusion limit of transport equations derived from velocity-jump processes*, *SIAM J. Appl. Math.*, 61 (2000), pp. 751–775.
- [24] T. HILLEN, K. J. PAINTER, M. WINKLER, AND A. D. MURTHA, *Moments of von Mises and Fisher distributions and applications*, *Mathematical Biosciences and Engineering*, 14 (2017), pp. 673–694, <https://doi.org/10.3934/mbe.2017038>.
- [25] D. HOLCMAN AND Z. SCHUSS, *The narrow escape problem*, *SIAM Review*, 56 (2014), pp. 213–257, <https://doi.org/10.1137/120898395>.
- [26] S. A. IYANIWURA AND Z. PENG, *Mean first passage time of active Brownian particles in two dimensions*, *New Journal of Physics*, 27 (2025), p. 104401.
- [27] R. A. JANNAT, M. DEMBO, AND D. A. HAMMER, *Neutrophil adhesion and chemotaxis depend on substrate mechanics*, *J. Phys.: Condens. Matter*, 22 (2010), p. 194117.
- [28] K. KEREN ET AL., *Mechanism of shape determination in motile cells*, *Nature*, 453 (2008), pp. 475–480.
- [29] A. KLAR, *The Milne problem for high field kinetic equations*, *SIAM Journal on Applied Mathematics*, 64 (2004), pp. 757–772, <https://doi.org/10.1137/S0036139902408898>.
- [30] V. KURELLA, J. C. TZOU, D. COOMBS, AND M. J. WARD, *Asymptotic analysis of first passage time problems inspired by ecology*, *Bulletin of mathematical biology*, 77 (2015), pp. 83–125.
- [31] S. D. LAWLEY, *Universal formula for extreme first passage statistics of diffusion*, *Physical Review E*, 101 (2020), p. 012413, <https://doi.org/10.1103/PhysRevE.101.012413>.
- [32] J. LEE ET AL., *Principles of locomotion for simple-shaped cells*, *Nature*, 362 (1993), pp. 167–171.
- [33] R. L. LINDQUIST, G. SHAKHAR, D. DUDZIAK, H. WARDEMANN, T. EISENREICH, M. L. DUSTIN, AND M. C. NUSSENZWEIG, *Visualizing dendritic cell networks in vivo*, *Nature Immunology*, 5 (2004), pp. 1243–1250, <https://doi.org/10.1038/ni1139>.
- [34] P. MAIURI ET AL., *Actin flows mediate a universal coupling between cell speed and cell persistence*, *Cell*, 161 (2015), pp. 374–386.
- [35] K. V. MARDIA AND P. E. JUPP, *Directional Statistics*, Wiley, 2000.
- [36] M. J. MILLER ET AL., *Two-photon imaging of lymphocyte motility and antigen response in intact lymph node*, *Science*, 296 (2002), pp. 1869–1873.
- [37] M. J. MILLER ET AL., *Autonomous T cell trafficking examined in vivo with intravital two-photon microscopy*, *Proc. Natl. Acad. Sci. USA*, 100 (2003), pp. 2604–2609.
- [38] H. G. OTHMER AND T. HILLEN, *The diffusion limit of transport equations ii: Chemotaxis equations*, *SIAM Journal on Applied Mathematics*, 62 (2002), pp. 1222–1250, <https://doi.org/10.1137/S0036139900382772>.

-
- [39] G. A. PAVLIOTIS, *Stochastic Processes and Applications: Diffusion Processes, the Fokker–Planck and Langevin Equations*, vol. 60 of Texts in Applied Mathematics, Springer, 2014, <https://doi.org/10.1007/978-1-4939-1323-7>.
- [40] M. J. PLANK, M. J. SIMPSON, AND R. E. BAKER, *Random walk models in the life sciences: including births, deaths and local interactions*, *Journal of the Royal Society Interface*, 22 (2025), p. 20240422.
- [41] A. QUARTERONI, R. SACCO, AND F. SALERI, *Numerical Mathematics*, Springer, 2 ed., 2007.
- [42] L. N. TREFETHEN AND J. A. C. WEIDEMAN, *The exponentially convergent trapezoidal rule*, *SIAM Rev.*, 56 (2014), pp. 385–458.
- [43] P. J. M. VAN HAASTERT AND L. BOSGRAAF, *Food searching strategy of amoeboid cells by starvation induced run length extension*, *PLoS ONE*, 4 (2009), p. e6814.

Supplementary Figures

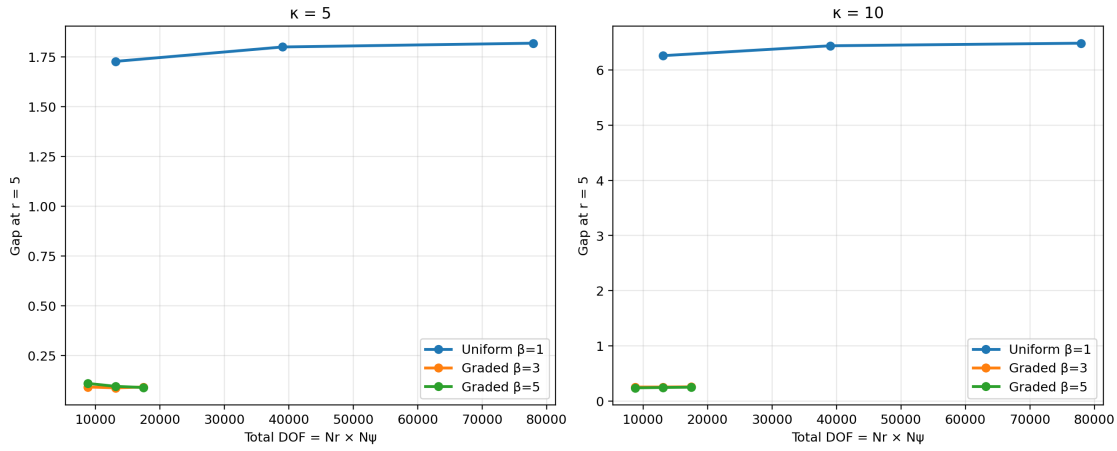


Figure 10: Direct-vs-Monte-Carlo relative gap at $r = 5$ on uniform and power-law graded radial meshes, as a function of total angular plus radial degrees of freedom $N_r \times N_\psi$. These two values bracket the regime boundary: $\kappa = 5$ is the upper end of the biologically relevant range and the hardest case the production solver must resolve, while $\kappa = 10$ lies in the strong-persistence regime where the wall layer falls below the minimum graded mesh cell width. Three mesh families are compared at $N_\psi = 144$, $\Delta\tau = 0.007$: uniform ($\beta = 1$), graded $\beta = 3$, and graded $\beta = 5$. At $\kappa = 5$, graded $\beta = 3$ collapses the near- R wall error by more than an order of magnitude at fixed total DOF and is essentially flat under further refinement, justifying its choice as the production setting; graded $\beta = 5$ gives no additional benefit and drives Δr_{\min} toward machine epsilon.

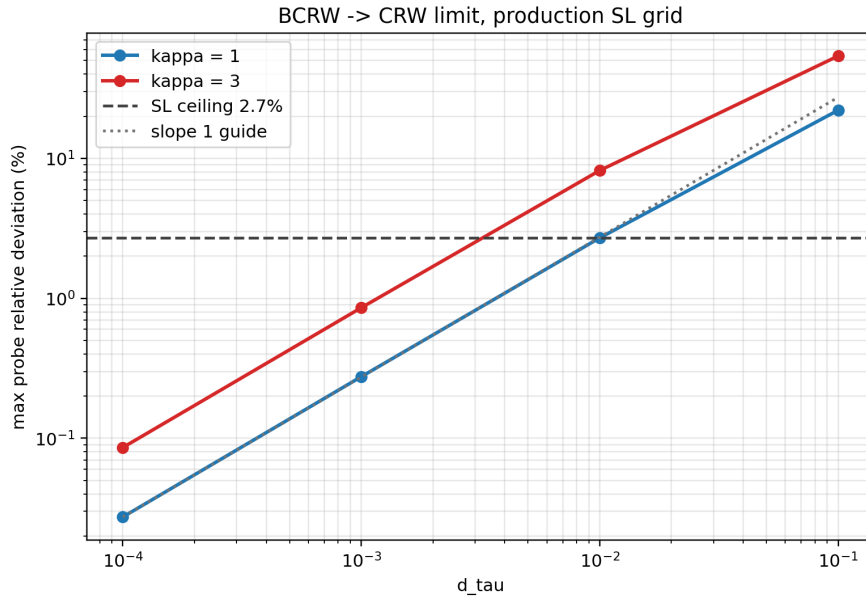


Figure 11: BCRW-to-CRW consistency check at the production semi-Lagrangian grid ($\beta = 3$, $N_r = 121$, $N_\psi = 144$, $a = 1$, $R = 5$, $s = 1$, $\mu = 3$). Plotted is the maximum probe relative deviation $|\bar{T}_{\text{BCRW}} - \bar{T}_{\text{CRW}}|/\bar{T}_{\text{CRW}}$ over the four probe radii $r \in \{1.5, 2.5, 3.5, 5\}$, as a function of bias strength d_τ , for $\kappa = 1$ (lymphocyte range) and $\kappa = 3$ (fibroblast range). The dashed line marks the semi-Lagrangian structural ceiling at 2.7%; the dotted line is a slope-1 reference. Fitted slopes are 0.997 and 0.990 respectively, confirming the $O(d_\tau)$ scaling expected from the kernel expansion. The crossover with the structural ceiling near $d_\tau \approx 10^{-2}$ sets the bias range over which the BCRW and unbiased CRW solvers can be compared directly.